

# FULL WAVE SIMULATION OF LARGE SATELLITE FOR THE EVALUATION OF MULTIPLE FREQUENCY ANTENNAS INTERFERENCE.

Benedetta Fiorelli<sup>(1)</sup>, Erik Jørgensen<sup>(2)</sup>

<sup>(1)</sup> ESA/ESTEC, Keplerlaan 1, NL-2200 AG Noordwijk, The Netherlands, Email: Benedetta.Fiorelli@esa.int

<sup>(2)</sup> TICRA, Landemærket 29, DK-1119 Copenhagen, Denmark, Email: ej@ticra.com

## ABSTRACT

The paper presents a full wave simulation of the spacecraft of JUICE, ESA's Jupiter Icy moons Explorer mission. Results prove the possibility of simulating the entire spacecraft modelling the instruments of the payload in a realistic environment to predict unwanted interference and consequent unexpected RF behaviour that would be impossible to be foreseen by either stand-alone or simplified configuration of the antennas on board.

The simulations are performed making use of the new full wave analysis tool available in TICRA's GRASP and show the capability of the software to deal with complex structures producing reliable results. The direct CAD import makes the tool very attractive in terms of modelling effort vs computational time.

## 1. INTRODUCTION

Large satellites typically embark complex payloads which include several instruments working at different frequencies. As mass and space are strong constraints for any space mission, payloads are characterized by high level of integration of different components and a smart and effective collocation of several antennas within the same limited available area on the platform.

In this framework, the RF interaction prediction is very complex and requires an accurate evaluation. The antennas can interfere with each other depending on the operational bandwidth and the satellite itself can cause unwanted reflections.

While at initial design stages each antenna can be modelled as stand-alone, the final evaluation of the antenna performances will need to take into account the satellite environment.

It is well known that a full wave simulation represents a significant step forward to the full satellite's interaction and instrument performance evaluation and it leads to a much better insight of the RF behaviour of the satellite and its instruments as a whole. While the potential of such an approach is clearly recognised, the feasibility and the accuracy of the results are the actual challenges. Given the size of a satellite and the number of instruments typically embarked, the RF problem is usually very large in terms of wavelengths. Simplified models have been an inevitable choice in the past since commercial tools were unable to deal with the required level of complexity. These simplifications lead to a

certain level of approximation and may underestimate important contributions. Moreover, the implementation and test of simplified models can be very time consuming.

Commercial software packages are constantly being improved in terms of computational capability and have been lately enhanced to explore the possibility of feeding the simulator with the actual full CAD model of the satellite. The goal is to cope with the need of a full wave simulation of very large and complex structures to be set and run in a reasonable amount of time to produce reliable results.

In this paper the new full-wave solver from TICRA's GRASP software is used to simulate and analyse a full satellite based on direct import of CAD models. The software and its new features are described in Section 2. The case of study is the spacecraft of the ESA's mission JUICE[1] briefly introduced in Section 3 for a general overview in the specific context of this work. Finally the results are presented in Section 4 and Section 5.

## 2. NEW HIGHER-ORDER MLFMM SOLVER IN GRASP

The full-wave analysis tool used in this paper is based on the higher-order MoM solver available in TICRA's GRASP software. This solver was recently extended in an ARTES 5.2 activity [2] to enable accurate analysis of electrically large structures with modest CPU time and memory requirements. The improved algorithms allowing this improvement are described below.

Full-wave solutions to electrically large radiation and scattering problems are usually obtained by solving an integral equation for the unknown surface currents on the object. The standard solution approach is based on the Method of Moments (MoM) and the unknown surface current is discretized with RWG basis functions. The Multi-Level Fast Multipole Method (MLFMM) is used to reduce the memory and CPU time from  $O(N^2)$  to  $O(N \log N)$ . This approach is used in nearly all commercial solvers based on integral equations.

The RWG discretization typically requires 130 unknowns per square wavelength to achieve the desired solution accuracy. In contrast to this, a smoother discretization using higher-order basis functions can readily achieve the same accuracy with only 30 unknowns per square wavelength [3].

Unfortunately, the standard MLFMM scheme leads to quite poor performance when applied in conjunction with higher-order basis functions due to the larger

geometrical extent of the basis functions. A new HO-MLFMM scheme tailored to higher-order basis functions was proposed recently [4] and implemented in the higher-order MoM solver in GRASP. The computational savings made available by this new solver are shown quantitatively in the next section. Furthermore, the new solver also employs an innovative formulation that allows the use of non-connected meshes, which is described in a subsequent section, 2.2

### 2.1. Memory and CPU performance of the new solver

When MLFMM is applied to MoM-based discretizations with different expansion orders, there is no direct link between the number of basis functions and the solution error. Therefore, it is more illustrative to study the required computational resources versus the solution error since this shows how one can minimise the error for a given set of resources.

In order to study the solution error we compare the CFIE HO-MLFMM results with the exact solution for a sphere with a diameter of 50 wavelengths. A fixed polynomial order  $p$  between 1 and 5 is applied on meshes with different patch densities and the memory, CPU time, and solution error are recorded for each run. The plot in Figure 1 shows the results for the memory performance for both a standard MLFMM [5] and the HO-MLFMM [4].

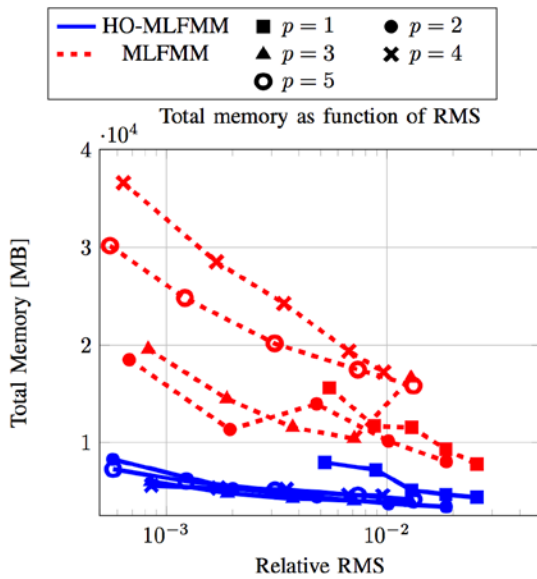


Figure 1. Total memory consumption as a function of the relative RMS error achieved.

As anticipated in the previous section, Figure 1 shows that the standard MLFMM scheme does not work well with higher-order expansion functions and the memory requirement grows when the order is increased. Moreover, memory requirement grows rapidly if high accuracy is desired. On the other hand, the HO-MLFMM algorithm provides memory savings even for

first-order basis functions and all expansion orders higher than one results in roughly the same memory requirement to reach a desired error level. Being the memory curve flat, almost the same amount of memory is required when asking for higher accuracy.

The total memory usage shown in Figure 1 would suggest that there is no real benefit from using high expansion orders in MLFMM-based solvers. However, this is not the case as it is shown in Figure 2 where the CPU time required per matrix-vector product is plotted as a function of relative RMS. It is shown that the fastest solution is always obtained by choosing the highest possible expansion order for both MLFMM and HO-MLFMM.

In summary, the HO-MLFMM algorithm allows for an efficient solver using less memory and CPU time than other integral-equation based solvers.

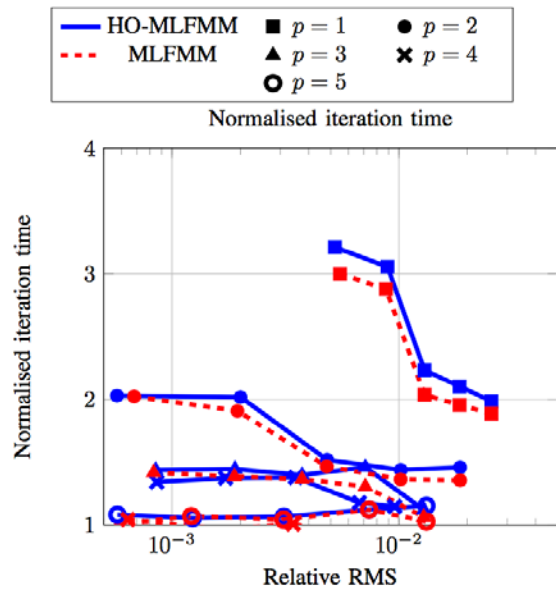


Figure 2. Normalised time per matrix-vector product as a function of the relative RMS error achieved.

### 2.2. Mesh Robustness

The accuracy and convergence properties of integral-equation based solvers are heavily influenced by the quality of the surface mesh. It is of primary importance to build a geometrical model that gives the right information to the solver to build the mesh. The type of input that each solver can handle to produce an efficient mesh in terms of accuracy and computational time is related to the implemented algorithm.

By far the majority of integral-equation based solvers make use of the mixed-potential EFIE that requires continuous basis functions. In this case the meshes must be properly connected for the entire model to guarantee the required continuity. Such a constraint may create problems when meshing complex structures and requires time-consuming modifications of the model. It is particularly challenging when the geometry is

imported from a CAD file with wrong or missing topological information that will result in a mesh without proper connectivity. The new solver circumvents the mesh connectivity problem by using a generalized set of surface integral equations that allows the use of non-connected meshes [6]. This enables independent meshing of each face in a complex model. The obtained surface currents will flow continuously between faces as long as the edges are not separated more than a defined tolerance. The concept is illustrated in Figure 3 that shows the surface current obtained on a complicated shape represented by a non-connected mesh.

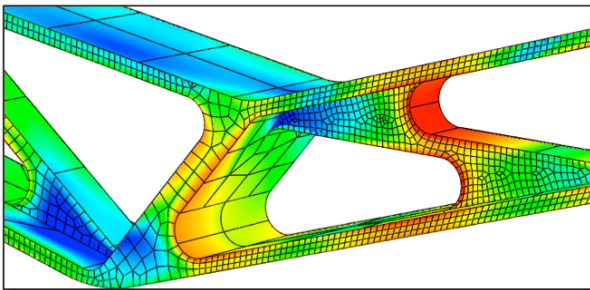


Figure 3. Currents obtained on a non-connected mesh.

Typical CAD cleaning tasks are still required and need to be performed in a CAD tool before importing the model into GRASP. They include removing electrically small parts and identifying possible overlapping parts. Electrically small parts result in a potentially large computational overhead without adding significant contributions. Overlapping parts cannot be handled by the solver and such parts are therefore indicated visually by GRASP, which allows the user to identify the offending parts to be modified in a CAD tool.

### 3. CASE OF STUDY: JUICE

The Jupiter Icy moons Explorer is a Large-class mission in ESA's Cosmic Vision 2015–2025 programme. Planned for launch in 2022 and arrival at Jupiter in 2030, it will spend at least three years making detailed observations of the biggest planet Jupiter and three of its largest moons, Ganymede, Callisto and Europa. It will visit Callisto and will fly by Europa twice. JUICE will make the first measurements of the thickness of Europa's icy crust and will identify candidate sites for future in situ exploration. The spacecraft will enter orbit around Ganymede where it will study the icy surface and internal structure of the moon, including its subsurface ocean.

JUICE will be equipped with 10 instruments, including cameras, spectrometers, an ice-penetrating radar, an altimeter, radio-science experiments, and sensors to monitor the magnetic fields and charged particles. One further experiment will combine data from the spacecraft telecommunication system and ground-based

instruments.

JUICE will embark instruments for several experiments:

- JANUS: Optical camera system;
- MAJIS: Moons and Jupiter Imaging Spectrometer, visible and infrared;
- UVS: UV Imaging Spectrograph;
- SWI: Sub-millimetre Wave Instrument;
- GALA: Ganymede Laser Altimeter;
- RIME: Radar for Icy Moons Exploration;
- J-MAG: Magnetometer for JUICE;
- PEP: Particle Environment Package;
- RPWI: Radio & Plasma Wave Investigation;
- 3GM: Gravity & Geophysics of Jupiter and Galilean Moons.

Moreover, additional antennas will be used for the satellite TMTC and communication to ground.

In the radio frequency band the receiving and transmitting antennas together will cover most of the spectrum from a few MHz up to hundreds of GHz making use of different technologies to realise low-, medium- and high-gain antennas.

#### 3.1. Satellite model and antennas under study

It is worth highlighting at this point that the satellite model used in this study is based on the best knowledge of the authors. Dimensions, positions and details of the different parts of the satellite are subject to changes and they may differ from what presented in this paper. The goal of this study is in fact to show the possibility of analysing the complex structure of the satellite to give input during the future design iterations.

Within the large set of antennas embarked on JUICE, two of them are selected to incorporate a reasonable range of frequencies in the analysis: RIME and the X-band low gain antennas.

RIME is the radar instrument to study surface structure of the Jupiter moons down to 9 Km in depth. The dipole antenna is designed to work at 9 MHz with 3 MHz bandwidth realizing an omnidirectional pattern. In our model the dipole is 40 mm in diameter and deploys perpendicularly to the solar panels which are about 30 m wide (Figure 4).

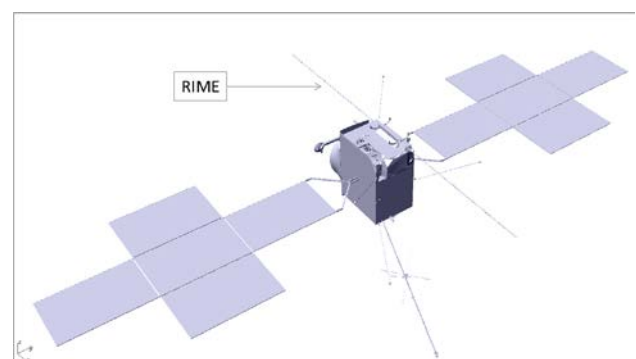


Figure 4. View of the satellite – RIME.

As the length of the dipole is comparable with the solar panel size and because more filar antennas are installed on the satellite body, the interaction of the dipole with the rest of the spacecraft needs to be analysed.

The X-band LGAs location are selected to produce omnidirectional coverage from the satellite, Figure 5. They are aimed at transmitting and receiving to the ground station on Earth. The frequency considered in this study is 8.4GHz.

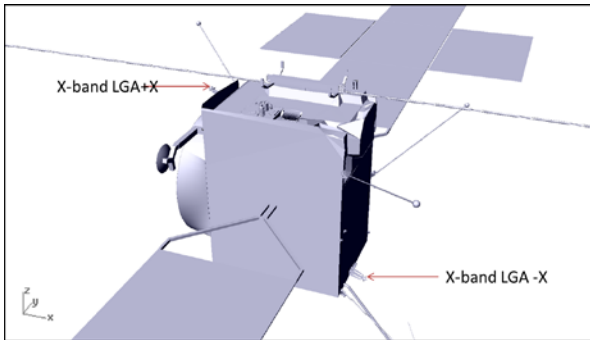


Figure 5. View of the satellite – X-band LGAs.

Both LGAs are located in a way to minimize the interaction with the spacecraft. Nevertheless, it is not possible to completely avoid the effects of the surroundings on the hemispherical pattern of the low gain antenna. For this reason it is especially important to be able to characterize the antennas on the spacecraft.

#### 4. RESULTS: RIME

To run a full wave simulation of the satellite, a model was built starting from CAD files of the satellite body including the MLI, solar panels and antennas. The CAD was cleaned taking into account the electrical dimensions of the details in order to produce the most efficient computational model. As described in Section 2.2, the continuity of the mesh is not required with the new HO-MLFMM solver in GRASP. However, the very low frequency of 9 MHz makes it challenging to obtain a mesh that accurately represents the geometry while at the same time requires as few patches as possible and avoids electrically tiny patches. The resulting mesh includes small patches with a side length of wavelength/1000 which was set as the smallest acceptable size. The final meshing takes about 10 seconds at 9MHz and it is shown in Figure 6 with the calculated currents produced by feeding the dipole with a voltage generator.

The dipole was simulated in 4 different positions with respect to the S/C moving it along the z-axis to increase the distance of the feeding point to the S/C as shown in Figure 7. The nominal position is assumed for this study to be 50 mm away from the S/C as the dipole is above of the support that protects the dipole before deployment. The distance was increased by 150mm, 200mm and 300mm. The goal is to study how the

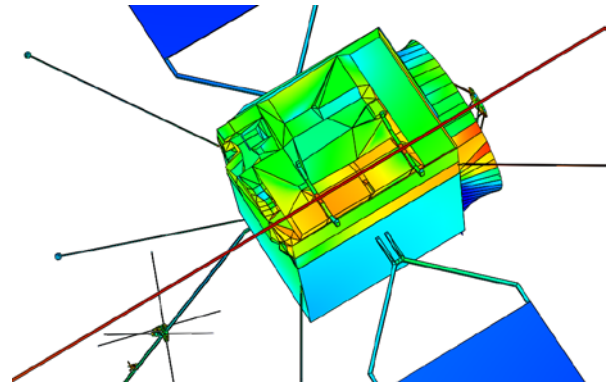


Figure 6. Mesh and current distribution at 9MHz.

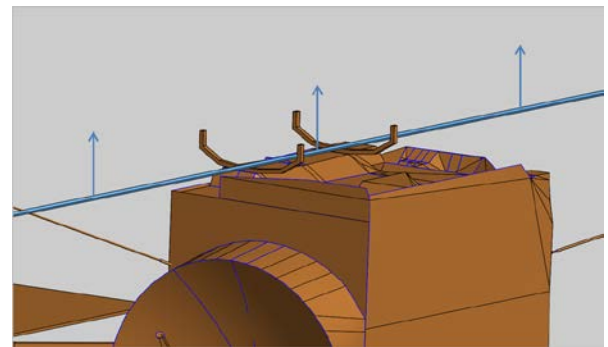


Figure 7. RIME dipole shift along z-axis.

matching at the feeding point changes to collect information for the design of the matching network. The radiation pattern cuts in the xz- and yz-plane are shown in Figure 8 and Figure 9 respectively for the four configurations. It can be noticed that the radiation pattern in the xz-plane is tilted a few degrees. This is due to the interaction with the S/C and in particular due to the asymmetric position of the dipole from the centre of the S/C in the xy-plane. The shift along the z axis of the dipole does not produce any effect on the radiation pattern as all four curves overlap.

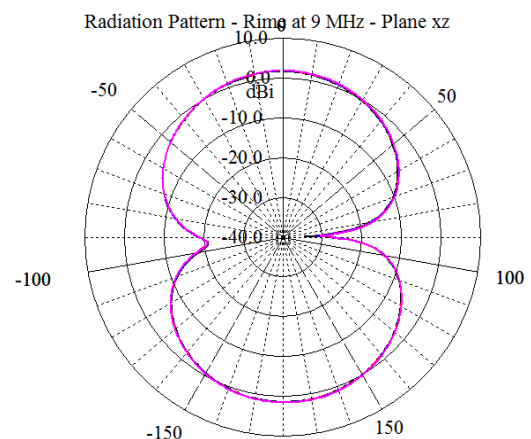


Figure 8. RIME radiation pattern cut in xz-plane.

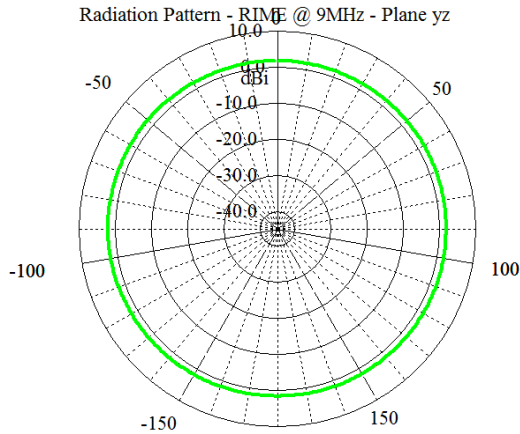


Figure 9. RIME radiation pattern cut in yz-plane.

Figure 10 shows the reflection coefficient at the feeding point of the RIME dipole in the four configurations. The S/C body acts as a ground plane and increasing the distance of the dipole from the S/C shifts the resonance down in frequency. It is worth noticing that the effect of the resonance is strictly related to the geometry of the S/C body in the region of the feeding point and the correct evaluation of such an effect can be properly evaluated only by taking into account the complex environment around it. The analysis is an important input for the matching network design.

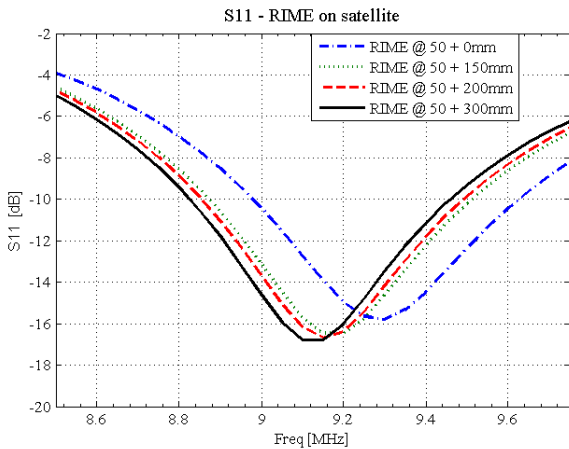


Figure 10. Reflection coefficient at RIME feeding point. Dipole at 0 mm, 150 mm, 200 mm and 300 mm from the nominal position in the z-axis.

## 5. RESULTS: X-band LGAs

Similar to the simulation described in previous section, a model of the satellite was built to obtain a mesh in X-band. The selected frequency is 8.4 GHz and a mesh was obtained at this frequency. The resulting model with the corresponding current generated by the X-band LGA+X (Figure 5) is shown in Figure 11. The dominant patch size in the mesh is  $1.5 \times 1.5$  wavelengths which is suitable for the HO-MLFMM in GRASP. Despite the large patch size, the electrically large platform results in

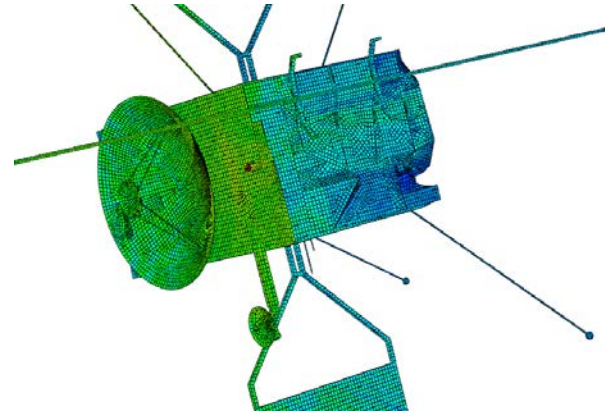


Figure 11. Mesh in X-band and currents distribution induced by LGA+X.

a fine mesh that is clearly in Figure 11 as well as the currents induced on the S/C by the LGA.

In order to evaluate the influence of the S/C on the radiation pattern, the X-band antenna was first simulated stand-alone in free space. The excitation is defined as two voltage generators in phase quadrature that feed two small wires inside the antennas to realize a circular polarized feed. The radiation pattern is shown in Figure 12. The antenna produces a hemispherical pattern in circular polarization.

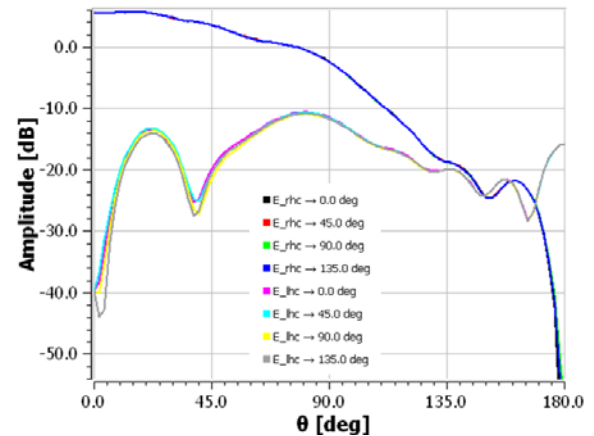


Figure 12. X-band LGA stand-alone

The radiation pattern was then simulated for the X-band LGA+X integrated on the S/C. Figure 13 shows the radiation pattern for both the RHC and LHC (cross-pol) in xz-plane ( $\phi=0^\circ$ ) of the coordinate system of the antenna (shown in Figure 14). Ripples in the pattern of the LGA+X on S/C are visible for both RHC and LHC components. When compared to the LGA stand-alone (dotted line) the asymmetry of the pattern is clearly visible due to the presence of the large reflector and S/C body, i.e for  $-90^\circ < \theta < 150^\circ$ . The effect of the presence of the S/C is visible in other field pattern cuts but is not shown here for brevity.

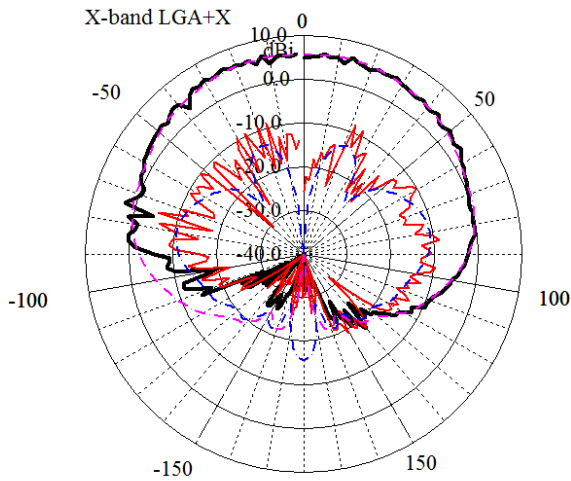


Figure 13. LGA+X antenna pattern in the xz plane of the antenna. RHC and LHC components. On S/C: solid line. In FS: dashed line.

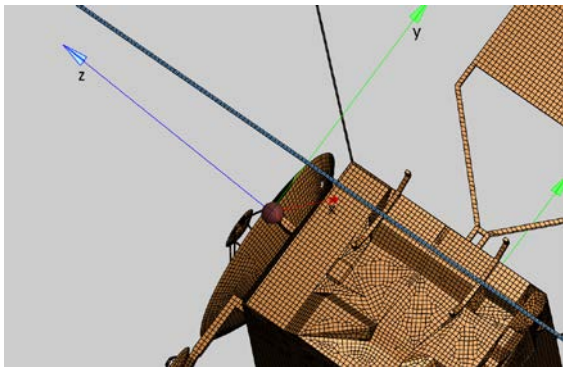


Figure 14. LGA+X coordinate system.

The LGA-X was simulated using the same model of the S/C as the LGA+X. As the two LGAs are aimed at realizing an omnidirectional coverage, they are located in opposite position with respect to the S/C. As a matter of fact they interact with different instruments and portion of the S/C body and need to be investigated separately. In Figure 15 the mesh and current distribution are shown as induced by the LGA-X. The interaction with the S/C and the filar antennas in the region illuminated by the LGA-X is visible. Figure 17 shows the radiation pattern cut at  $\phi=135^\circ$  in the coordinate system of the LGA-X (shown in Figure 16). The specific cut has been selected to show the effect on the LGA-X radiation pattern of the 3m LANGMUIR probe, J-MAG boom (6.7 m) and RPWI dipoles (2.5 m). The effect of the S/C is present in cuts but it is not shown here for brevity.

Ripples of the pattern are observed for both the RHC and LHC component. The cross-pol level increases significantly and the pattern symmetry is visibly distorted in the region for  $300^\circ < \theta < 360^\circ$ . The effect of the presence of the MAG boom at  $\theta \sim -50^\circ$  is clearly visible. A zoom of Figure 17 is presented in Figure 18

where the degradation of the pattern up to 3dB can be appreciated.

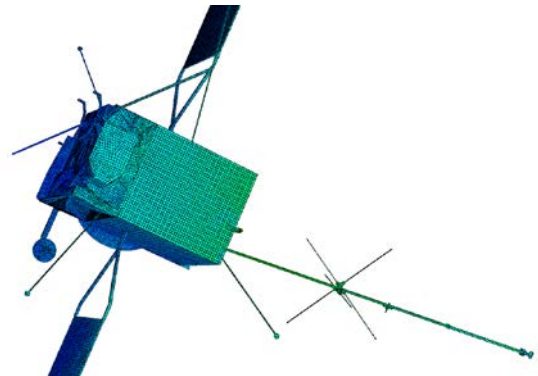


Figure 15. Mesh in X-band and currents distribution induced by LGA-X.

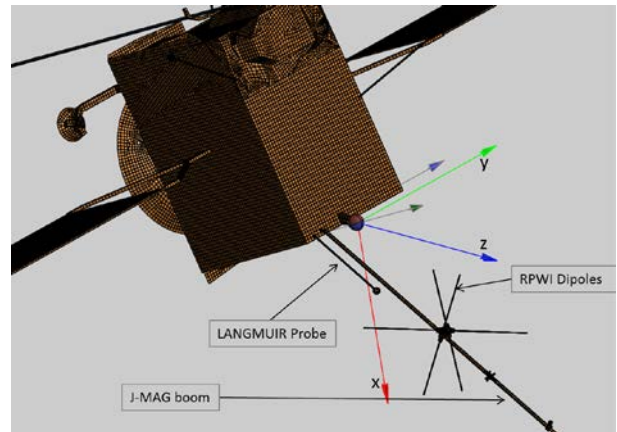


Figure 16. LGA-X coordinate system.

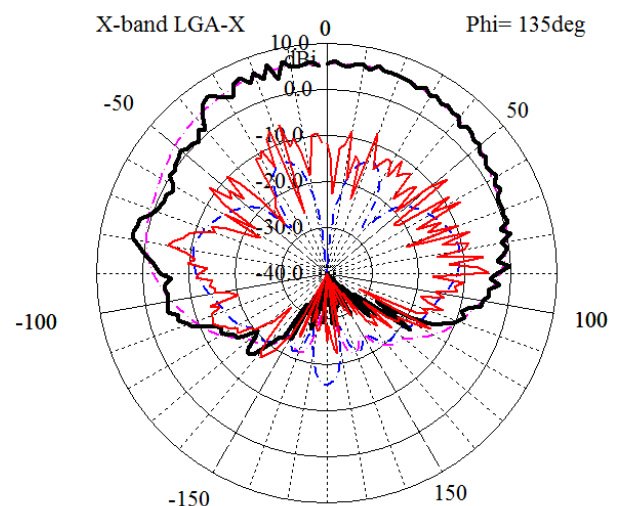


Figure 17. LGA-X antenna pattern cut at  $\phi=135^\circ$  in the coordinate system of the antenna. RHC and LHC components. On S/C: solid line. In FS: dashed line.

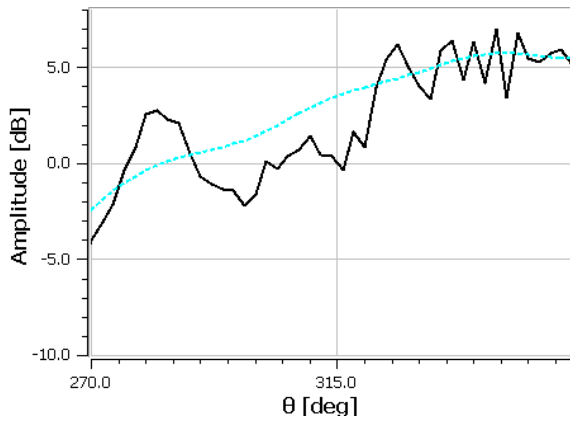


Figure 18. LGA-X antenna pattern cut at  $\phi=135^\circ$  in the coordinate system of the antenna. On S/C: solid line. In FS: dashed line. Pattern degradation in the region  $270^\circ < \theta < 360^\circ$

## 6. CONCLUSIONS

A full wave simulation of a large satellite was presented in HF and X-band making use of the HO-MLFMM solver available in TICRA's GRASP. The case of study is JUICE. Results prove that the antennas embarked and their mutual interaction can be analysed taking into account the complex environment. It allows a reliable understanding of the RF behaviour of the S/C as a whole. Examples of the effect of the surroundings on the antennas performance were presented showing significant deviations from the predicted pattern at antenna design level. A full wave analysis of a large satellite, without resorting to a highly simplified model of the S/C, is considered a precious input for the antenna and S/C design iteration and a step forward in reliability and confidence level of the RF performances of the instruments.

## 7. REFERENCES

1. <http://sci.esa.int/juice/>
2. Jørgensen, E., Vesterdal, N., Meincke, P. & Borries, O. (2015). Integrated Tool for Reflector Antenna Design, Antenna Farm Scattering, and Interference Prediction, *ESTEC Contract 4000107963, Final Report*. TICRA, Copenhagen, Denmark.
3. Jørgensen, E., Volakis, J.L, Meincke, P. & Breinbjerg, O. (2004), Higher-Order Hierarchical Legendre Basis Functions for Electromagnetic Modeling, *IEEE Trans. Antennas Propagat.*, **52**(11), 2985—2995.
4. Borries, O., Meincke, P., Jørgensen, E. & Hansen, P.C. (2014), `Multilevel Fast Multipole Method for Higher Order Discretizations, *IEEE Trans. Antennas Propagat.* **62**(9), 4695 – 4705.
5. Song, J.M. & Chew, W.C. (1995). Multilevel Fast-Multipole Algorithm for Solving Combined Field Integral Equations of Electromagnetic Scattering, *Microwave and Optical Technology Letters*, **10**(1), 14—19.
6. Peng, Z., Lim, K.-H. & Lee, J.-F. (2013), A Discontinuous Galerkin Surface Integral Equation Method for Electromagnetic Wave Scattering From Nonpenetrable Targets, *IEEE Trans. Antennas Propagat.*, **61**(7), 3617—3628.
7. <http://sci.esa.int/juice/50073-science-payload/>
8. Bruzzone, L., Alberti, G., Catallo, C., Ferro, A., Kofman, W. & Orosei, R. (2011). Subsurface Radar Sounding of the Jovian Moon Ganymede. *Proceedings of the IEEE* (Volume:99 , Issue: 5 ) pp. 837 - 857.
9. Bruzzone, L., Plaut, J.J., Alberti, G., Blankenship, D.D., Bovolo, F., Campbell, B.A.; Ferro, A., Gim, Y., Kofman, W., Komatsu, G., McKinnon, W., Mitri, G., Orosei, R., Patterson, G.W., Plettemeier, D., Seu, R. (2013) RIME: Radar for Icy Moon Exploration. In Proc. *Geoscience and Remote Sensing Symposium (IGARSS), 2013 IEEE International*. Pp. 3907 – 391.
10. Di Paolo, F. Cosciotti, B. ; Lauro, S.E. ; Mattei, E. ; Pettinelli, E. ; Vannaroni, G.